Factors Controlling the Diversities of MJO Propagation and Intensity

Tianyi Wang^{a,b} and Tim Li^{a,b}

^a Key Laboratory of Meteorological Disaster, Ministry of Education, Joint International Research Laboratory of Climate and Environmental Change, Collaborative Innovation Center on Forecast and Evaluation of Meteorological Disasters, Nanjing University of Information Science and Technology, Nanjing, China

(Manuscript received 9 November 2020, in final form 11 May 2021)

ABSTRACT: The diversity of the Madden–Julian oscillation (MJO) in terms of its maximum intensity, zonal extent, and phase speed was explored using a cluster analysis method. The zonal extent is found to be significantly correlated to the phase speed. A longer zonal extent is often associated with a faster phase speed. The diversities of zonal extent and speed are connected with distinctive interannual sea surface temperature anomaly (SSTA) distributions and associated moisture and circulation patterns over the equatorial Pacific. An El Niño–like background SSTA leads to enhanced precipitation over the central Pacific, allowing a stronger vertically overturning circulation to the east of the MJO. This promotes both a larger east—west asymmetry of column-integrated moist static energy (MSE) tendency and a greater boundary layer moisture leading, serving as potential causes of the faster phase speed. The El Niño–like SSTA also favors the MJOs intruding farther into the Pacific, causing a larger zonal extent. The intensity diversity is associated with the interannual SSTA over the Maritime Continent and background moisture condition over the tropical Indian Ocean. An observed warm SSTA over the Maritime Continent excites a local Walker cell with a subsidence over the Indian Ocean, which could decrease the background moisture, weakening the MJO intensity. The intensity difference between strong and weak events would be amplified due to distinct intensity growth speed. The faster intensity growth of a strong MJO is attributed to a greater longwave radiative heating and a greater surface latent heat flux, both of which contribute to a greater total time change rate of the column-integrated MSE.

KEYWORDS: Madden-Julian oscillation; Intraseasonal variability; Tropical variability

1. Introduction

The Madden–Julian oscillation (MJO) is the dominant intraseasonal mode of tropical atmosphere. It was first discovered by Madden and Julian (1971, 1972), but the detection of the tropical 40–50-day signal could be traced back to Xie et al. (1963) [see a recent review by Li et al. (2018)]. The MJO exerts significant impacts on global weather and climate across different spatial and temporal scales (Zhang 2005, 2013; Li et al. 2020), and therefore serves as a major predictability source for subseasonal forecast (Vitart et al. 2017; Kim et al. 2018; Wang et al. 2020). Thus, it is of great importance to understand the physical mechanisms of MJO.

The MJO is generally characterized by a large-scale envelope of convective anomalies that propagates slowly eastward along the equator, with a principal period of 30–60 days and zonal wavenumbers of 1–3 (Madden and Julian 1994; Li 2014). The active convection and enhanced subsidence anomaly in the front cause a horizontal Rossby–Kelvin wave couplet pattern of MJO (Rui and Wang 1990; Wang and Li 1994; Hendon and Salby 1994). The boundary convergence in the front and the upper-level stratiform clouds in the rear form a westward-tilted vertical structure of MJO (Sperber 2003; Lin et al. 2004; Hsu and Li 2012; Wang et al. 2017).

Currently a widely accepted theory for explaining MJO propagation is the moisture mode theory. The hypothesis behind

thesis behind primarily from the enhanced boundary layer convergence, which is contributed by both Kelvin wave response and warmer sea surface temperature anomalies (SSTAs).

It is worth noticing that the dominant processes in both types of moisture mode theory are associated with the general

this theory is that processes controlling the zonal asymmetry of the moisture or moisture tendency hold a key for the

propagation, while the symmetric component (relative to

the MJO convection) is critical for intensity change. After

years of development, the moisture mode theory can be well

separated into two types (Li et al. 2020; L. Wang and Li

2020; Hu et al. 2021). The first type emphasizes the asym-

metry of the column-integrated moist static energy (MSE)

tendency anomaly (Maloney 2009; Raymond and Fuchs

2009; Sobel and Maloney 2013; Kim et al. 2014; Adames and

Kim 2016; Wang et al. 2017; Li and Hu 2019; T. Wang and Li

2020). The advections of background MSE by the meridio-

nal and vertical intraseasonal flows are dominant processes

that contribute to the east-west asymmetry of MSE ten-

dency in MJO. The meridional advection is associated with

the Rossby wave response to MJO convection and subsi-

dence perturbations (Kim et al. 2014; Adames and Kim

2016), while the asymmetry of the vertical advection is

mainly attributed to the upper-level stratiform clouds in the

rear of deep convection (Wang et al. 2017; Li and Hu 2019).

The second type of moisture mode theory emphasizes the

boundary layer moisture anomaly leading (Hsu and Li 2012;

T. Wang et al. 2018). The accumulation of the boundary

layer moisture to the east of the MJO convection results

Corresponding author: Tim Li, timli@hawaii.edu

DOI: 10.1175/JCLI-D-20-0859.1

^b International Pacific Research Center and Department of Atmospheric Sciences, School of Ocean and Earth Science and Technology, University of Hawaii at Mānoa, Honolulu, Hawaii

structures of the MJO, namely, the horizontal Rossby-Kelvin wave couplet and the westward-tilted vertical structure. This implies that the MJO propagation and intensity characteristics would be sensitive to its own structure change, while the latter could be modulated by the background states. Actually, the year-to-year changes of the MJO activities have early been noticed (Lau and Chan 1986; Gutzler and Madden 1989; Gutzler 1991; Salby and Hendon 1994). Later studies unveiled the variabilities of MJO in terms of many aspects, such as the zonal extent or life cycle (e.g., Fink and Speth 1997; Hendon et al. 1999; Tam and Lau 2005; Kim et al. 2014; Feng et al. 2015a; Suematsu and Miura 2018), the propagation speed (e.g., Tam and Lau 2005; Pohl and Matthews 2007; Izumo et al. 2010; Chen et al. 2016; Wei and Ren 2019; Chen and Wang 2020), and the intensity (e.g., Pohl and Matthews 2007; Feng et al. 2015b; Chen et al. 2016; Deng et al. 2016; L. Wang et al. 2018). Most of the studies argue that the MJO variabilities are strongly modulated by the interannual changes of tropical SSTAs.

The variabilities of MJO in terms of its zonal extent, propagation speed, and intensity imply the complexity of individual MJO events. A recent study by Wang et al. (2019) proposed the concept of diversity of MJO. They applied a cluster analysis to the Hovmöller diagrams of MJO events to objectively group the MJOs into four clusters. According to the propagation characteristics revealed by the composite Hovmöller diagrams, the four clusters are referred to as standing, jumping, slow, and fast. They argue that the tight coupling between the Kelvin wave response and the MJO convection distinguishes the propagating and nonpropagating events, while the strength and length of Kelvin wave response determine the speed. The background SSTAs over the tropical Pacific affect the MJO diversity by modifying the Kelvin wave response.

The four clusters suggested by Wang et al. (2019) distinguish the individual MJO events from each other in terms of their propagation characteristics, but such a clustering failed to capture the diversity of the MJO intensity. It is also arguable whether the standing and jumping types correspond with the definition of MJO which emphasizes the eastward propagating. We speculate that although the Hovmöller diagrams contain information regarding both propagation and intensity, the latter is not expressed in a concentrated and explicit manner such that the diversity of propagation might stand out in the cluster analysis. Meanwhile, those nonpropagating or westward-propagating signals are also contained in the temporal-filtered Hovmöller diagrams.

Inspired by the pilot work of Wang et al. (2019), we would like to conduct a more comprehensive study on the diversity of MJO, in which both propagation and intensity diversities are addressed. As a powerful tool used by Wang et al. (2019), the cluster analysis would also be adopted as a key to classify different types of MJOs. But rather than the Hovmöller diagrams, we attempt to use only a few variables to describe and cluster the MJO events, such that the information regarding the propagation and intensity would be more concentrated and more equally weighted. A spatial–temporal filter would be applied to extract the eastward-only signals. The factors controlling the MJO propagation and intensity diversities would

be explored from the aspect of MJO internal dynamics under the framework of moisture mode theory, and from the aspect of background states.

The rest of the paper is organized as follows. Section 2 introduces the data and methods. Section 3 describes how the MJO events are identified and the diversities of MJO unveiled by the cluster analysis. Sections 4 and 5 explore what factors control the MJO propagation and intensity diversities, respectively. A summary is given in section 6.

2. Data and methods

a. Data and preprocessing

The datasets used in this study are 1) the observed daily outgoing longwave radiation (OLR) from the National Oceanic and Atmospheric Administration (NOAA) (Liebmann and Smith 1996); 2) the ERA5 from the European Centre for Medium-Range Weather Forecasts (Hersbach et al. 2020); and 3) the Group for High Resolution Sea Surface Temperature (GHRSST) Level 4 AVHRR_OI Global Blended Sea Surface Temperature Analysis (GDS2) from NCEI, version 2.1 (Reynolds et al. 2007). The OLR data have a $2.5^{\circ} \times 2.5^{\circ}$ spatial resolution. The raw ERA5 dataset is available at hourly with a $0.25^{\circ} \times 0.25^{\circ}$ spatial resolution, and has been averaged into daily and $2.5^{\circ} \times 2.5^{\circ}$ resolutions in this study. The sea surface temperature data are daily at a $0.25^{\circ} \times 0.25^{\circ}$ spatial resolution. The period of 1979/80 to 2018/19 boreal winters (from November to April) is used in the research.

The climatological annual cycle of 1981–2010 has been removed to obtain the anomalous components. To extract the MJO-scale intraseasonal anomalies, a bandpass filter with a passband of 20–80 days in period has been applied. In addition, the eastward-propagating components with zonal wavenumbers 1–9 of the intraseasonal OLR anomalies are filtered out to identify the MJO events. A detailed description will be given in section 3a.

b. Cluster analysis and diagnostic methods

Following Wang et al. (2019), the cluster analysis (Kaufman and Rousseeuw 2005; Everitt et al. 2011; Wierzchon and Klopotek 2018) is used to objectively examine the diversity of the MJO. Both hierarchical clustering and *k*-means clustering are tested to group the selected MJO events into a few clusters, based on three different properties regarding the intensity and propagation of the MJO. A detailed description will be given in section 3b.

To unveil the dynamic causes of the MJO propagation and intensity diversities, the MSE budget diagnosis is conducted. The moist static energy M at a constant pressure level is defined as

$$M \equiv C_p T + L_e q + gz, \tag{1}$$

where T is the air temperature, q is the specific humidity, z is the geopotential height, C_p is the specific heat capacity at constant pressure (=1004J K⁻¹ kg⁻¹), L_e is the latent heat of vaporization (=2.5 × 10⁶ J kg⁻¹), and g is the gravitational acceleration (=9.8 m s⁻²). Following Neelin and

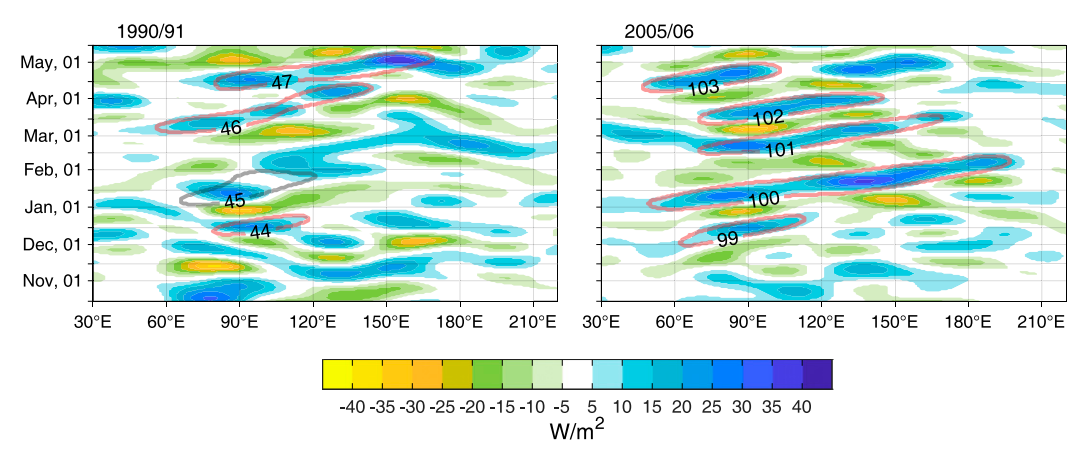


Fig. 1. Hovmöller diagrams of intraseasonal (20–80-day-filtered) OLR anomalies (shading) averaged over 15° S– 10° N during the (left) 1990/91 and (right) 2005/06 boreal winters. The $-10\,\mathrm{W\,m^{-2}}$ contours of the eastward-propagating component with zonal wavenumbers 1–9 of the intraseasonal OLR anomalies are superimposed, which indicate the candidate MJO events and are labeled by sequence numbers. The gray contour denotes the excluded event due to its larger deviation between spatially filtered and nonfiltered intraseasonal OLR anomalies, whereas the red contours denote the selected cases.

Held (1987), the column-integrated MSE budget equation can be written as

$$\langle \partial_t M \rangle' = -\langle V \cdot \nabla_h M \rangle' - \langle \omega \partial_p M \rangle' + \langle Q_r \rangle' + Q_t', \qquad (2)$$

where V is the horizontal wind vector, ∇_h is the horizontal gradient operator, ω is the vertical pressure velocity, p is the pressure, Q_r represents the sum of the shortwave and longwave radiative heating, and Q_t represents the sum of the surface upward sensible and latent heat fluxes. The angle brackets represent a mass-weighted vertical integration from the surface to 100-hPa level. To diagnose the MSE budget on the MJO time scale, a 20–80-day bandpass filter (denoted by a prime) is applied to Eq. (2).

To identify the relative contributions of different time scales and their nonlinear interaction effects in the intraseasonal MSE budget, a decomposition method similar to that used in Hsu and Li (2012) and Li et al. (2015) is applied:

$$X = \overline{X} + X' + X^*,\tag{3}$$

where X represents any time-dependent variable, and is decomposed into a low-frequency component (>80 days, denoted by an overbar), an intraseasonal component (20–80 days, denoted by a prime), and a high-frequency component (<20 days, denoted by an asterisk). It is worth noticing that the low-frequency component represents the slow-varying background of intraseasonal oscillations, which contains the climatological annual cycle, the interannual to multidecadal variabilities, and long-term trends.

c. Composite procedure

The lead-lag composite analyses are achieved by aligning the MJO events at the moment when convection maximizes (referred to as day 0). In most cases, the MJO convection center is located over the eastern Indian Ocean (around 90°E)

at day 0. The statistical significance of composite anomalies was assessed by a two-tailed Student's *t* test at the 90% or 95% confidence level. For composites of each individual cluster, the null hypothesis is that the composites have equal means of the climatology. For composites of differences between two clusters, the null hypothesis it that the two clusters have equal means. A statistically significant result indicates the rejection of the null hypothesis.

3. Cluster analysis for MJO propagation and intensity diversities

a. Identifications of individual MJO events

Following Kiladis et al. (2014), the MJO events are identified with the spatial-temporal-filtered OLR anomalies in this study. Given that the MJO is defined as an eastward-propagating intraseasonal oscillation, an intraseasonal eastward-only filter is applied to the OLR anomalies averaged between 15°S and 10°N. Here the period of 20-80 days and the eastward-propagating component with zonal wavenumbers 1-9 are retained. The eastward wavenumber filtering is only applied in MJO events identification, but not the composite analyses below. The latitudinal range is asymmetric about the equator because the MJO paths tend to shift southward during boreal winter (Wang and Rui 1990; Zhao et al. 2013; Kim et al. 2017). In the Hovmöller diagrams of such spatial-temporal-filtered OLR anomalies, a -10 W m⁻² contour (about one standard deviation of the intraseasonal OLR over the MJO active area; Feng et al. 2015a) is selected as a candidate MJO event, as long as it falls in boreal winter (November to April) and overlaps the eastern Indian Ocean region (75°-95°E), and has a zonal extent of more than 30° in longitude. An example is shown in Fig. 1, in which the contours denote the candidate MJO events during 1990/91 and 2005/06 winters.

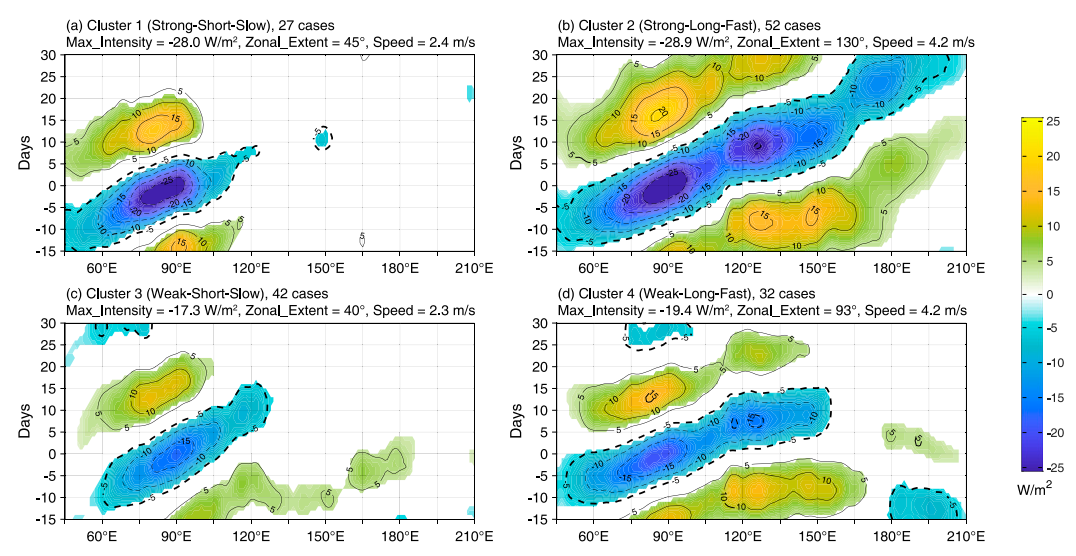


FIG. 2. (a)—(d) Hovmöller diagrams of composite intraseasonal OLR anomalies averaged over 15°S–10°N during boreal winter (November–April) for clusters 1–4, respectively. The shading shows statistically significant signals at 95% confidence level. The name of the cluster and number of events, together with the maximum intensity, zonal extent, and mean phase speed of the composite are displayed above each panel.

The criterion of the final identification of an MJO event from the candidates is that the spatial-temporal-filtered and temporal-only-filtered signals must be consistent with each other. By examining the candidate MJO events, we find that the spatial filtering occasionally produces unrealistic eastward-propagating signals that largely deviate from the temporal-only-filtered signals. Case 45 shown in Fig. 1 is an example. Although the spatial-temporal filtering obtains a successive eastward-propagating signal (contour) in this case, the temporal-filtered intraseasonal OLR anomalies (shading) during the same period are interrupted and rather propagating westward. We use the ratio of the mean OLR inside the contour obtained from the two different filtering methods to estimate such a deviation. For a candidate MJO event, if such a ratio is greater than one standard deviation of all the candidates, it is excluded. A total of 153 MJO cases are finally identified from 1979/80 to 2018/19 boreal winters.

b. Cluster analysis

The maximum intensity, zonal extent, and mean phase speed are used to describe the intensity and propagation characteristics of selected MJO cases, and further for analyzing their diversities. For an individual MJO event identified with the contour in the Hovmöller diagram, its maximum intensity is defined as the average of the lowest 10% of OLR values inside the contour, the zonal extent refers to the distance between the western and eastern endpoints of the contour, and the mean phase speed is estimated by the slope of the least squares fit of the daily minimum OLR inside the contour.

A cluster analysis is performed in terms of the maximum intensity, zonal extent, and mean phase speed of the selected MJO cases. Two different methods, hierarchical clustering and k-means clustering, are tested, with a variety of parameters

including the number of clusters, distance metrics, and linkage methods. By examining the dendrograms, we found an optimum clustering result given by the hierarchical clustering, whose number of clusters is 4, distance metric is Euclidean, and linkage method is Ward's (Ward 1963). An very similar result with a high silhouette value can be obtained by the *k*-means clustering, when the number of clusters is set to four and the distance metric is squared Euclidean. Therefore, such a clustering result with four cluster members is convincing and stable.

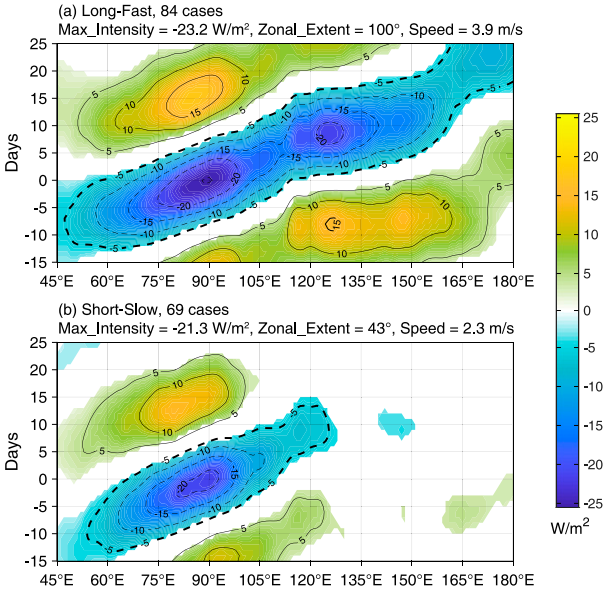


FIG. 3. As in Fig. 2, but for recombined (a) Long-Fast and (b) Short-Slow groups.

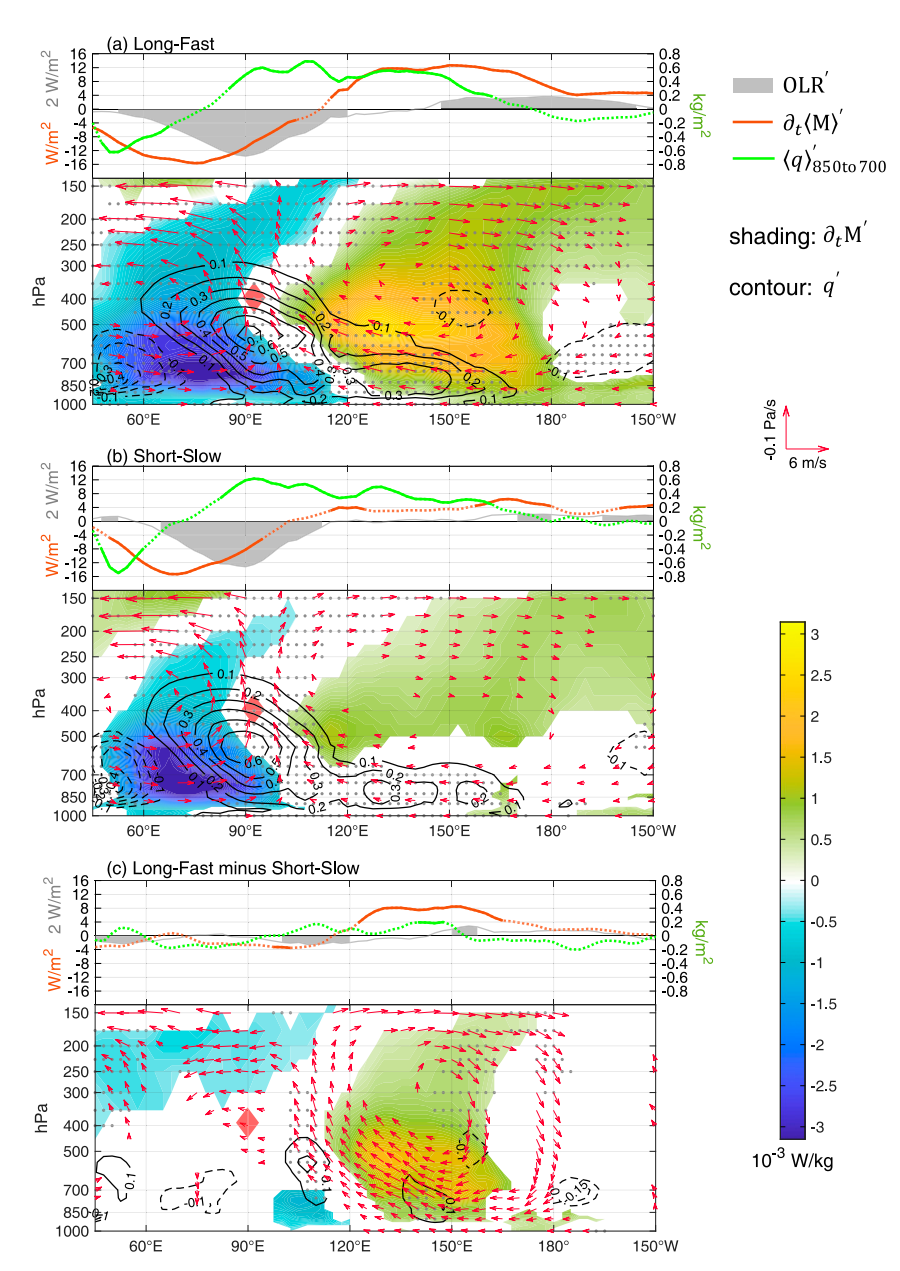


FIG. 4. Zonal distributions and longitude–height diagrams of composite intraseasonal anomalies averaged over $15^{\circ}\text{S}-10^{\circ}\text{N}$ for the (a) Long-Fast group, (b) Short-Slow group, and (c) Long-Fast group minus Short-Slow group. The one-dimensional plots on the top of each panel show the OLR (gray area), column-integrated MSE tendency (red lines), and 850–700-hPa vertically integrated water vapor content (green lines) anomalies. Filled areas and solid lines denote statistically significant signals at the 95% confidence level. The longitude–height diagrams at the bottom of each panel show the MSE tendency (shading), specific humidity (contours, in unit of g kg $^{-1}$), and vertically overturning circulation (vectors) anomalies. The shading, dotted areas of the contours, and vectors denote statistically significant signals at the 95% confidence level. The red diamonds denote the convection centers where the upward motions are the largest. For comparison, all the variables have been scaled to a same maximum intensity.

The composite Hovmöller diagrams of intraseasonal OLR anomalies (containing both eastward and westward wavenumbers, and the same below) for the four clusters obtained from the hierarchical clustering are shown in Fig. 2.

The maximum intensity, zonal extent, and mean phase speed of each cluster are calculated with this composite Hovmöller diagram. Based on these features, clusters 1 to 4 are labeled as "Strong-Short-Slow," "Strong-Long-Fast," "Weak-Short-Slow," and

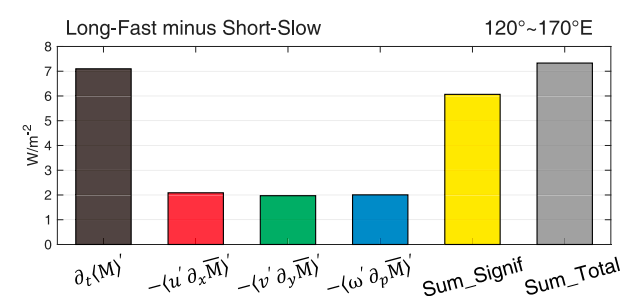


FIG. 5. Diagnosed results of column-integrated MSE tendency budget averaged over 15°S–10°N, 120°–170°E for the differences of composite intraseasonal anomalies between the Long-Fast and Short-Slow groups when the MJO deep convections are centered at 90°E. Bars from left to right denote the MSE tendency difference (black) and the three terms that significantly contributed to the difference (red, green, and blue), the sum of the three statistically significant terms (yellow), and sum of all the budget terms (gray). For comparison, all the terms in each group have been scaled to a same maximum intensity.

"Weak-Long-Fast," respectively. In other words, a cluster is either strong or weak in intensity, and is either short and slow or long and fast in propagation. Such a clustering result implies that the intensity and propagation characteristics of the MJO are relatively independent of each other, whereas regarding the propagation, a longer zonal extent is often associated a faster phase speed, which agrees with many of the previous studies (e.g., Wheeler and Kiladis 1999; Adames and Kim 2016; Chen and Wang 2019, 2020). Our calculation shows that for all the selected events, the linear correlation between the zonal extent and mean phase speed is 0.54 and is statistically significant at the 99% confidence level.

The clustering result shown in Fig. 2 clearly reveals the propagation and intensity diversities of the MJO. More importantly, it is found that the propagation and intensity characteristics are relatively independent. The four clusters can be regarded as a free combination of strong/weak and longfast/short-slow types of MJOs. In this case, we decided to recombine the four original clusters to study the MJO propagation and intensity diversities separately. That is, a new "Long-Fast" group is formed by combining the Strong-Long-Fast and Weak-Long-Fast clusters, and a new "Short-Slow" group is formed by combining the remaining two clusters, in order to study the MJO propagation diversity. Similarly, a new "Strong" group and a new "Weak" group are formed to study the MJO intensity diversity. The factors controlling the propagation and intensity diversities are discussed in the following sections, respectively.

4. Factors controlling the MJO propagation diversity

Figure 3 shows the composite Hovmöller diagrams of intraseasonal OLR anomalies for the recombined Long-Fast and Short-Slow groups. The two groups are significantly different from each other in terms of zonal extent and speed (100° vs 43° , and 3.9 vs $2.3\,\mathrm{m\,s^{-1}}$), whereas the maximum intensities are almost the same ($-23.2\,\mathrm{vs}-21.3\,\mathrm{W\,m^{-2}}$). In general, the Long-Fast MJOs passed through the Maritime Continent barrier (Inness and Slingo 2003; Zhang and Ling 2017) and dissipated over the central Pacific, whereas the Short-Slow MJOs failed to pass through the MC barrier and were confined over the Indian Ocean.

To examine the causes of the MJO propagation diversity, the key variables relevant to the two types of the moisture mode theory are diagnosed and compared for the Long-Fast

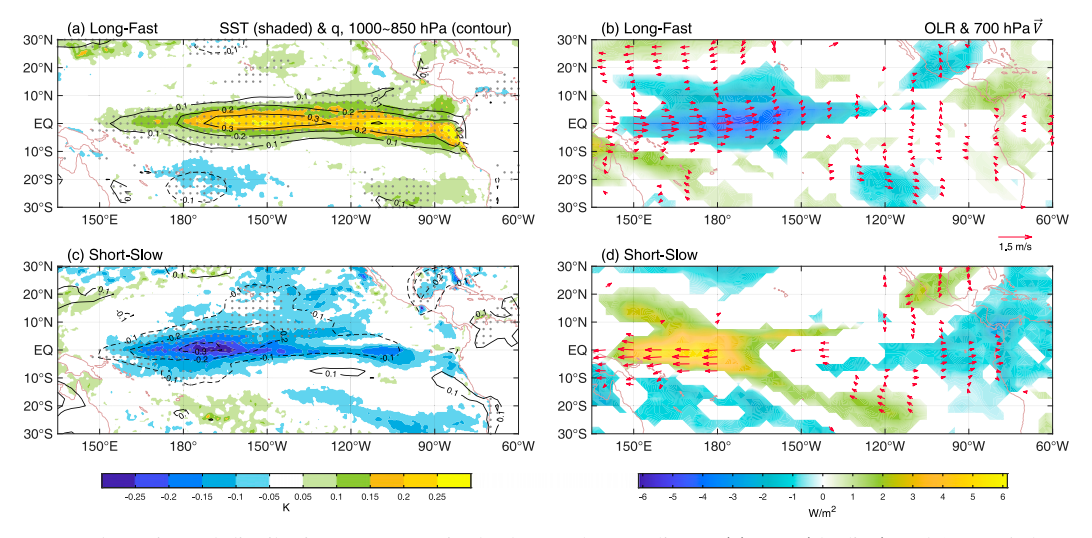


FIG. 6. Horizontal distributions of composite background anomalies of (a) SST (shading) and 1000-850-hPa vertically integrated water vapor content (contours; unit: $kg\,m^{-2}$) and (b) OLR (shading) and 700-hPa wind (vectors) for the Long-Fast group. (c),(d) As in (a) and (b), but for the Short-Slow group. The shading, dotted areas of the contours, and vectors denote statistically significant signals at the 90% confidence level. The background anomalies are 120-day low-pass filtered, and the composites are conducted for the entire life cycles of all the MJO events in each group.

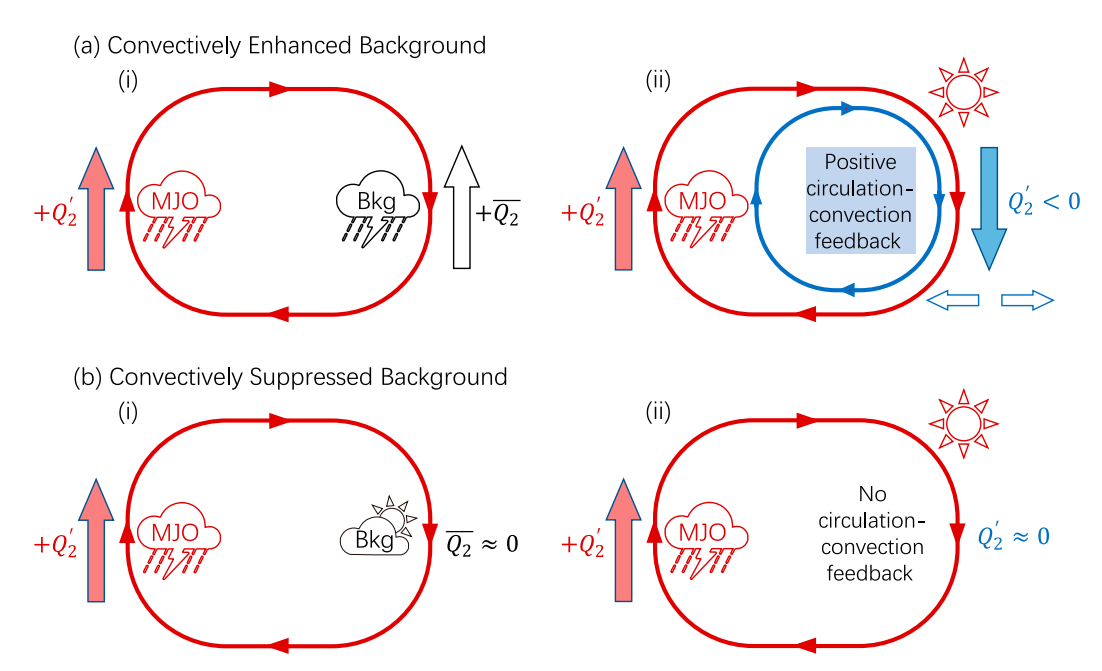


FIG. 7. Schematic diagram illustrating the enhancement of intraseasonal vertically overturning circulation anomaly through positive circulation–convection feedback in the existence of convective background. Closed cycles indicate vertically overturning circulations. Solid vertical arrows indicate latent heating. Unfilled horizontal arrows indicate boundary layer flows in response to the latent heating. Colored (black) elements refer to intraseasonal anomalies (background states). (a) In stage 1, an MJO convection over the Indian Ocean (red rainy icon and red solid arrow) excites a vertically overturning circulation anomaly (red cycle) whose subsidence branch is over the equatorial Pacific where the background is convective (black rainy icon). In stage 2, the latter reduces the total precipitation there and thus causes a negative diabatic heating anomaly ($Q_2' < 0$, blue solid arrow), forcing additional vertically overturning circulation (blue cycle) and divergent boundary layer flow (blue unfilled arrows). The initial red cycle is enhanced and a positive circulation–convection feedback is formed. (b) Under a convectively suppressed background (cloudy icon), an intraseasonal subsidence anomaly leads to a near-zero diabatic heating $(Q_2' \approx 0)$, and the circulation–convection feedback does not work.

and Short-Slow groups. Even though the maximum intensity difference is tiny between the two groups, for a better comparison all the variables in each group are scaled to a same maximum intensity (about $-25 \,\mathrm{W\,m^{-2}}$, which is the average of all four clusters).

Figure 4 shows that for both groups, when the MJO convection is mature over the eastern Indian Ocean (centered at 90°E), the vertically overturning circulation anomalies are formed to the west and east of the convection center, with low-level westerly (easterly) anomalies to the west (east), which corresponds with the Gill pattern (Gill 1980). The structure of the convection anomaly tilts westward with height, as indicated by the moisture and circulation anomalies. The east-west asymmetry of the MSE tendency anomalies and leading of boundary layer moisture anomalies relative to the MJO convection center are clearly identified, as argued in the moisture mode theory.

Several contrasts between the Long-Fast and Short-Slow groups are revealed in Fig. 4. A striking contrast is the much greater east—west asymmetry of the MSE tendency anomalies in the Long-Fast group relative to that in the Short-Slow group. It is found more clearly in the difference (Fig. 4c) that such a zonal asymmetry contrast is primarily determined by the MSE

tendency anomalies to the east of the MJO convection centers. In addition, a weak but statistically significant signal of larger boundary layer moisture anomaly leading in the Long-Fast group is detected at around 140°E. It is also noted that the anomalous vertically overturning circulation to the east of the MJO convection center is much stronger in the Long-Fast group, associated with more intense subsidence and low-level easterly anomalies to the east.

According to the moisture mode theory, both the greater MSE tendency leading and greater boundary layer moisture leading provide more favorable conditions for the eastward propagation of MJOs. For the Long-Fast case here, the first type of the moisture mode theory that emphasizes the asymmetry of the column-integrated MSE tendency anomaly plays a dominant role. Meanwhile, the role of the second type that emphasizes the boundary layer moisture anomaly leading cannot be completely denied.

To unveil what specific processes lead to the contrasts of the MSE tendency leading between the Long-Fast and Short-Slow MJOs, an MSE budget diagnosis is conducted. All the variables are decomposed into the low-frequency, intraseasonal, and high-frequency components according to Eq. (3) before diagnosing. The results of the differences between the two groups

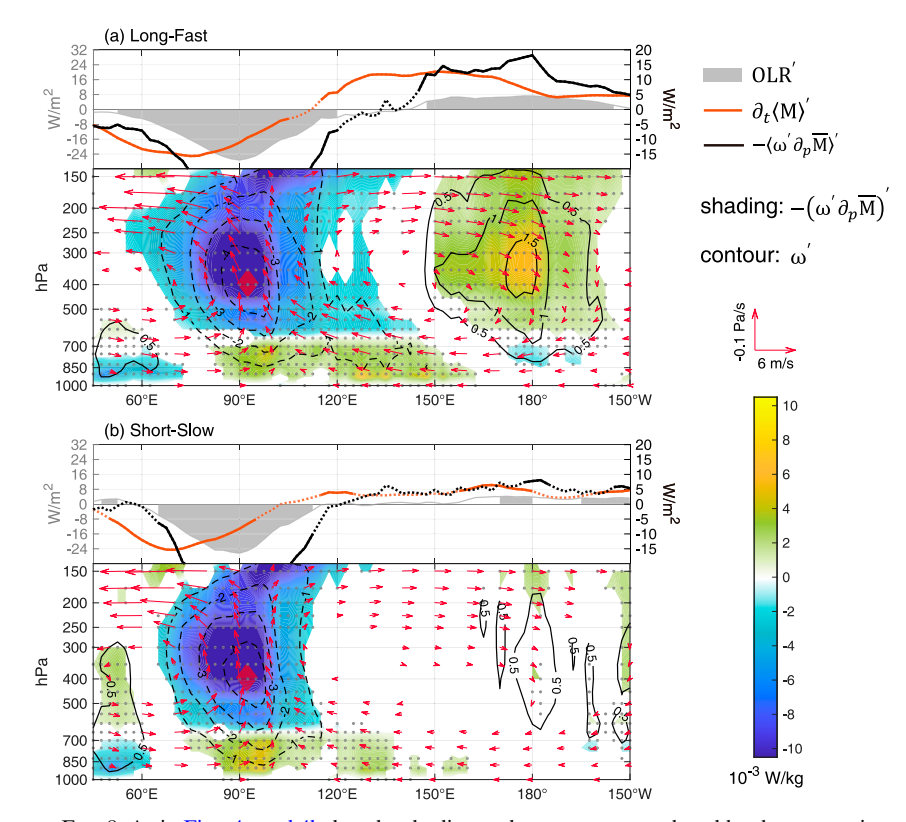


FIG. 8. As in Figs. 4a and 4b, but the shading and contours are replaced by the composite anomalies of vertical advection of background MSE by intraseasonal vertical motion and vertical pressure velocity (unit: Pa s⁻¹), respectively. The black lines in the one-dimensional plots represent the composite anomalies of column-integrated vertical advection of background MSE by intraseasonal vertical motion.

for the leading of column-integrated MSE tendency anomaly are shown in Fig. 5. Only those terms that significantly contribute to the difference are exhibited. They are simply the anomalous advections of background MSE by the intraseasonal flows, and the components of the three dimensions contribute almost equally. The sum of these statistically significant terms shows a good approximation.

The MSE budget diagnosis indicates that the contrast of the MSE tendency leading is related to the different intraseasonal circulation responses and background states. As mentioned before, the Long-Fast group has a much stronger vertically overturning circulation anomaly to the east of the convection center. Since all the variables are scaled to a same maximum intensity in the comparison, a new question is raised: What kind of background states causes the distinct circulation anomaly responses to the convection anomalies of the same intensity? And furthermore, how do the circulation anomalies and background states contribute to the distinct MSE tendency leading and boundary layer moisture leading?

To answer the above questions, the composite background anomalies of the Long-Fast and Short-Slow groups are examined. The background anomaly here refers to the 120-day low-pass-filtered anomaly, which is different from the low-frequency component in the MSE budget diagnosis.

The climatological annual cycle is removed in the former but retained in the latter. Thus, the background anomaly represents the slow-varying processes dominated by the interannual timescale.

Figure 6 shows that the Long-Fast MJOs correspond to a significant El Niño-like background SSTA pattern, accompanied

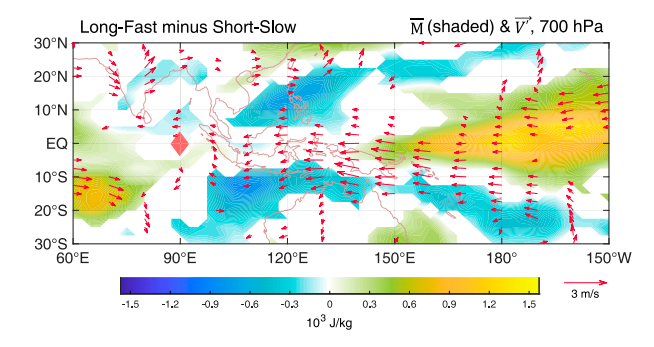


FIG. 9. Horizontal distributions of composite background MSE anomalies (shading) and intraseasonal circulation anomalies (vectors) at 700 hPa for the differences between the Long-Fast and Short-Slow groups. The shading and vectors displayed are statistically significant signals at the 90% confidence level.

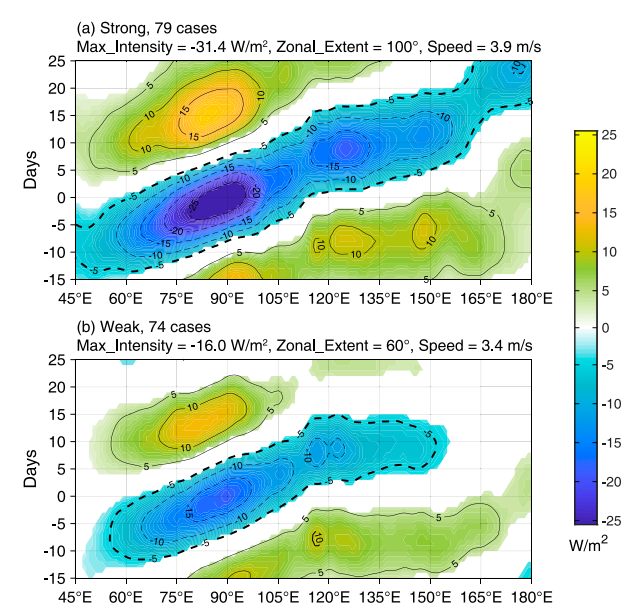


Fig. 10. As in Fig. 2, but for recombined (a) Strong and (b) Weak groups.

with increased low-level moisture and enhanced precipitation over the central Pacific. The Short-Slow group has almost opposite background states. Similar background SSTA patterns are also found in previous studies for faster MJOs (e.g., Wang et al. 2019; Wei and Ren 2019; Chen and Wang 2020). On one hand, the warmer background SSTA and more abundant moisture promote the MJOs to move farther into the eastern Pacific, so that the zonal extent would be larger in the Long-Fast group. On the other hand, the convective background over the central Pacific favors a stronger vertically overturning circulation response to the east of the MJO convection center, in which the negative diabatic heating anomaly and its positive feedback with the circulation are key processes.

The enhancement of the MJO vertically overturning circulation anomaly in the existence of convective background to

the east is illustrated in Fig. 7a. An initial subsidence anomaly to the east of the MJO convection causes a negative diabatic heating anomaly where the background convection is active. The resultant Gill response (Gill 1980) enhances the vertically overturning circulation anomaly to the east of the MJO convection. In addition, the exhibited upward moisture transport due to increased boundary layer divergence amplifies the initial subsidence anomaly and negative diabatic heating anomaly, such that a positive circulation-convection feedback is established. In contrast (Fig. 7b), when the background is convectively suppressed, an additional subsidence anomaly leads to a much smaller or even near-zero negative diabatic heating anomaly, simply because the total precipitation/cloud cover cannot be reduced to a negative value. It is also worth pointing out that a warmer background SSTA favors a stronger Kelvin wave response through boundary layer convergence feedback (Chen and Wang 2019), which also contributes to the enhancement of vertically overturning circulation.

The enhanced vertically overturning circulation in the Long-Fast group indicates a more intense subsidence anomaly to the east of the MJO convection center (Fig. 4, vectors; Fig. 8, contours and vectors). As pointed out in Wang et al. (2017), since the climatological MSE is minimized in the lower middle level, a stronger subsidence anomaly results in a larger positive advection of background MSE in the free atmosphere (Fig. 8, shading and black lines in the one-dimensional plots).

The enhanced vertically overturning circulation in the Long-Fast group also indicates a stronger Kelvin wave response and low-level easterly anomaly to the east of the MJO convection center (Figs. 4 and 9, vectors). Given that the background moisture in the Long-Fast group is increased over the central Pacific where the SSTA is warmer (Fig. 6a), the associated zonal advection of MSE would be greater since the strength-ened easterly anomaly transports higher background MSE (Fig. 9, shading) to the east of the MJO convection center. A larger low-level easterly anomaly also indicates an enhanced boundary layer convergence, and the moisture leading is thus increased (Hsu and Li 2012).

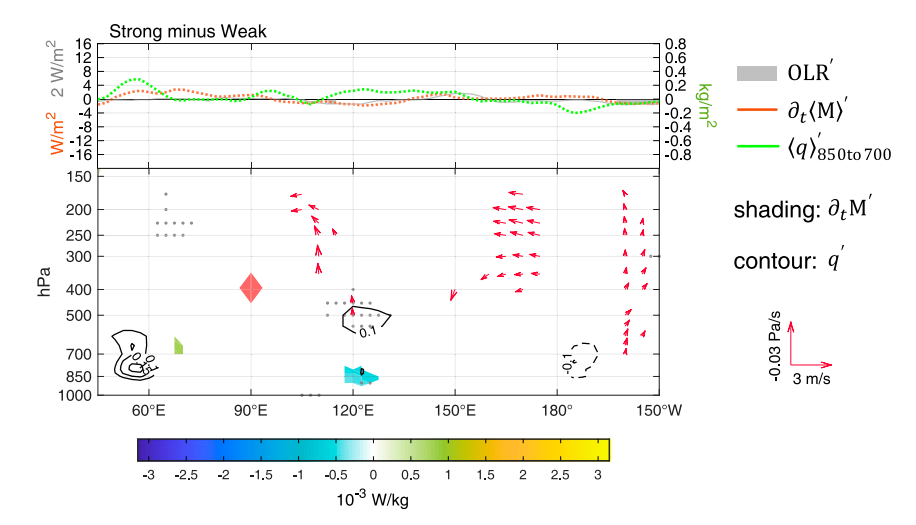


FIG. 11. As in Fig. 4, but for the differences between the Strong and Weak groups.

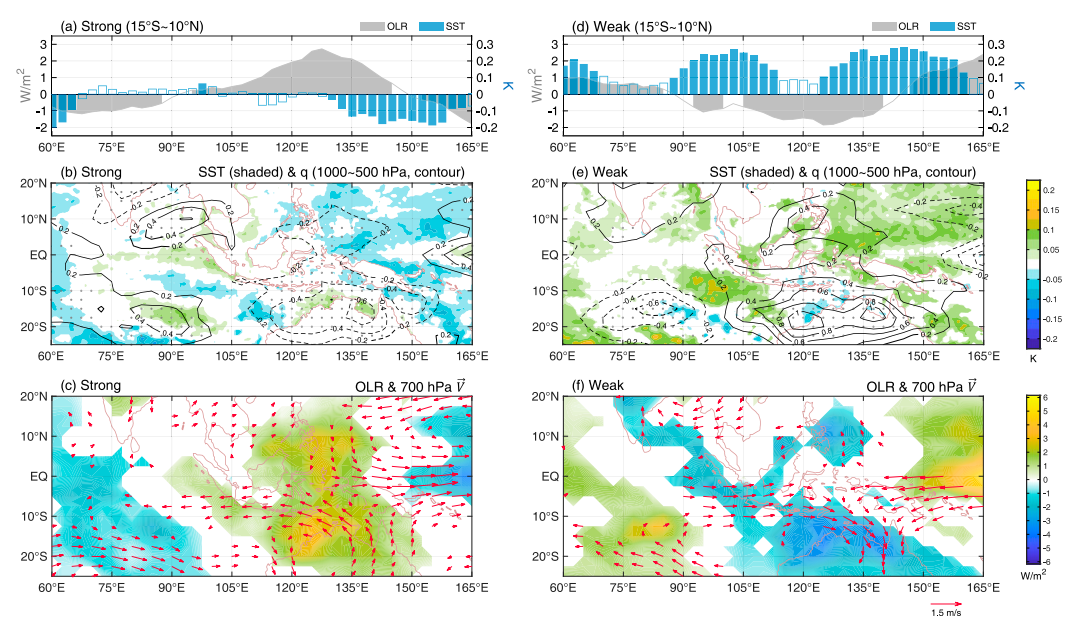


FIG. 12. Composite background anomalies for (a)–(c) Strong and (d)–(f) Weak groups. (a),(d) Zonal distributions of OLR (gray area) and SST (blue bars) averaged over 15°S–10°N. Filled areas and bars denote statistically significant signals at 90% confidence level. (b),(e) Horizontal distributions of SST (shading) and 1000–500-hPa vertically integrated water vapor content (contours; unit: kg m⁻²). (c),(f) Horizontal distributions of OLR (shading) and 700-hPa wind (vectors). The shading, dotted areas of the contours, and vectors denote statistically significant signals at the 90% confidence level.

The subsidence branch of the vertically overturning circulation anomaly causes a negative diabatic heating where the background is convectively enhanced in the Long-Fast group, and the resultant low-level Rossby wave response generates anomalous poleward flows to the east of the MJO convection center (Fig. 9, vectors around 120°E). Climatologically, the moisture is maximized near the equator. Such anomalous poleward flows contribute positively to the MSE tendency leading through meridional advection of background MSE, as discussed in Kim et al. (2014) and Wang et al. (2017). In the Long-Fast group, the background convective heating over the equatorial Pacific generates equatorward flows to the west as a Rossby wave response (Fig. 6b), such that the background moisture is more concentrated along the equator and the background MSE has a greater meridional gradient (Fig. 9, shading). In this case, the above-mentioned meridional advection effect would be much stronger in the Long-Fast group, as both the meridional gradient and poleward flows are increased.

5. Factors controlling the MJO intensity diversity

Figure 10 shows the composite Hovmöller diagrams of intraseasonal OLR anomalies for the recombined Strong and Weak groups. The two groups are significantly different from each other in terms of intensity that is maximized over the eastern Indian Ocean. The difference of propagation features between the Strong and Weak groups is much smaller in contrast to that between the Long-Fast and Short-Slow groups (Fig. 3). Particularly, although an apparent difference of the

zonal extent exists between the Strong and Weak groups, it is worth noticing that the statistically significant OLR signal of the composite Weak group passed through the Maritime Continent barrier, whereas the Short-Slow group failed. This implies that the Weak MJOs are intrinsically different from the Short-Slow ones (Kim et al. 2014; Feng et al. 2015a).

As we did in studying the MJO propagation diversity, the intraseasonal MSE tendency and boundary layer moisture anomalies are diagnosed and compared for the Strong and Weak groups when the MJO convections are mature over the eastern Indian Ocean. For comparison, all the variables are scaled to a same maximum intensity as before. Figure 11 reveals that as long as the variables are normalized in terms of the maximum intensity, there is almost no statistically significant difference between the Strong and Weak groups in terms of the MSE tendency, boundary layer moisture, and vertically overturning circulation anomalies. This suggests that the dynamic structures of the Strong and Weak MJOs are essentially the same, only their intensities are distinct.

The composite background anomalies (120-day low-pass filtered with climatological annual cycle removed) show distinct features between the Strong and Weak groups over the Indian Ocean and Maritime Continent. Figure 12 shows that the Weak MJOs correspond to warm background SSTA over the Maritime Continent and its surroundings, accompanied with more abundant low-level moisture and enhanced convective activities. The positive moisture and convection anomalies are shifting southward relative to the equator, which could result from the feedback with the Australian summer monsoon. A statistically significant low-level cyclonic circulation

anomaly appears over the Indian Ocean to the west of the enhanced convection, as a result of the Rossby wave response. The associated equatorward flow transports drier air to the tropical Indian Ocean and contributes to a statistically significant dry anomaly there. The background states of the Strong group are opposite in general.

The distinct background convective activities over the Maritime Continent also leads to different background vertical structures over the Indian Ocean between the Strong and Weak groups. Figure 13 shows the composite background anomalies of Weak minus Strong. A statistically significant Walker cell is detected, whose ascending is over the Maritime Continent where the background convection is enhanced and descending over the Indian Ocean. Such a subsidence anomaly also contributes to the background dry anomaly in the lower troposphere over the tropical Indian Ocean, in addition to the equatorward flow mentioned before. The resultant negative vertical gradient of the MSE anomaly indicates a convectively stable state over the Indian Ocean, which weakens the MJO intensity.

It is worth pointing out that an initial intensity difference due to the background could be amplified in the MJO eastward propagation. By tracking the MJO convection centers in Fig. 10, it can be found that a weak intensity difference appears between the Strong and Weak groups at the initial stage when the MJO convections are located over the western Indian Ocean. The different background is responsible for such an initial difference, as the dry anomaly and more stable stratification in the Weak group extend to the western Indian Ocean (Fig. 13). The intensity difference amplifies as the MJOs propagating eastward, and is maximized around day 0 when the MJO convections are located over the eastern Indian Ocean (around 90°E).

What causes the amplification of the initial intensity difference? We propose a self-feedback mechanism in terms of moisture mode theory, in which $d\langle M\rangle'/dt$ is focused rather than $\partial\langle M\rangle'/\partial t$, so as to depict the MJO intensity change per unit time following its propagation. In this case, the MJO intensity growth speed is determined by the diabatic processes except for condensation:

$$\frac{d\langle M\rangle'}{dt} = \langle Q_r\rangle' + Q_t',\tag{4}$$

where Q_r and Q_t represent the three-dimensional radiative heating, and sum of the surface upward sensible and latent heat fluxes, respectively.

The diagnosed results for the moments when $d\langle M\rangle'/dt$ are maximized (days -7 to -4 and MJO convections are located around 75°E) are shown in Fig. 14. Here Q_r is derived from $Q_1-Q_2-Q_t$ (Yanai et al. 1973). It is found that both $\langle Q_r\rangle'$ and Q_t' are contributing to the $d\langle M\rangle'/dt$ difference between the Strong and Weak groups. For the $\langle Q_r\rangle'$, a stronger MJO corresponds to more intense convections and therefore more cumulus congestus clouds. In addition, the Strong MJOs have a more significant upper-level tilted structure in the rear of the deep convection as depicted by the vertical velocity anomalies (Fig. 14, contours). Such a tilted structure suggests more stratiform clouds in the upper level (Lin et al. 2004). Both congestus and upper-level stratiform clouds inhibit the outgoing longwave radiation, such

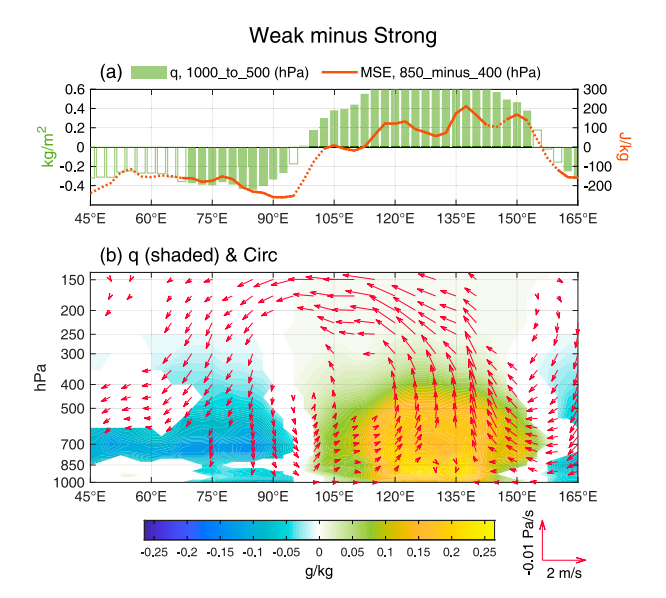


FIG. 13. Composite background anomalies for Weak group minus Strong group. (a) Zonal distributions of 1000–500-hPa vertically integrated water vapor content (green bars) and MSE difference between 850 and 400 hPa (red line) averaged over 15°S–10°N. Filled areas and solid lines denote statistically significant signals at the 90% confidence level. (b) Longitude–height diagram of specific humidity (shading) and vertically overturning circulation (vectors). The shading and vectors displayed are statistically significant signals at the 90% confidence level.

that larger positive radiative heating anomalies appear over the convective areas in the Strong group (Fig. 14, shading and red lines). On the other hand, the Strong MJOs correspond to higher near-surface wind speed, which is the dominant component that contribute to the Q_t' term (Fig. 14, green bars and lines). As both radiative heating and surface heat flux processes are regulated by the MJO intensity, a positive self-feedback thus forms to amplify the initial intensity difference during the propagation.

The above processes are essentially a combined cloud-radiative and WISHE (wind-induced surface heat exchange) feedback. Early studies applied the cloud-radiative feedback to explain the formation of standing intraseasonal oscillations (Hu and Randall 1994, 1995). The WISHE was also known as a potential eastward-propagating mechanism of the MJO under the assumption that the mean surface zonal wind is on average easterly in the tropics (Emanuel 1987; Fuchs and Raymond 2017; Fuchs-Stone 2020). Here both the cloud-radiative and WISHE feedbacks are in fact not contributing to the eastward propagation as there are no positive anomalies to the east of the MJO convection [see a comment by Wang (1988)]. Instead, they work as a positive feedback of the MJO intensity. Such a positive feedback holds regardless of whether the system is propagating or standing, since they contribute to the total derivative $d\langle M \rangle'/dt$.

6. Summary

Inspired by Wang et al. (2019), who unveiled the diversity of MJO propagation patterns, the current work conducted a more

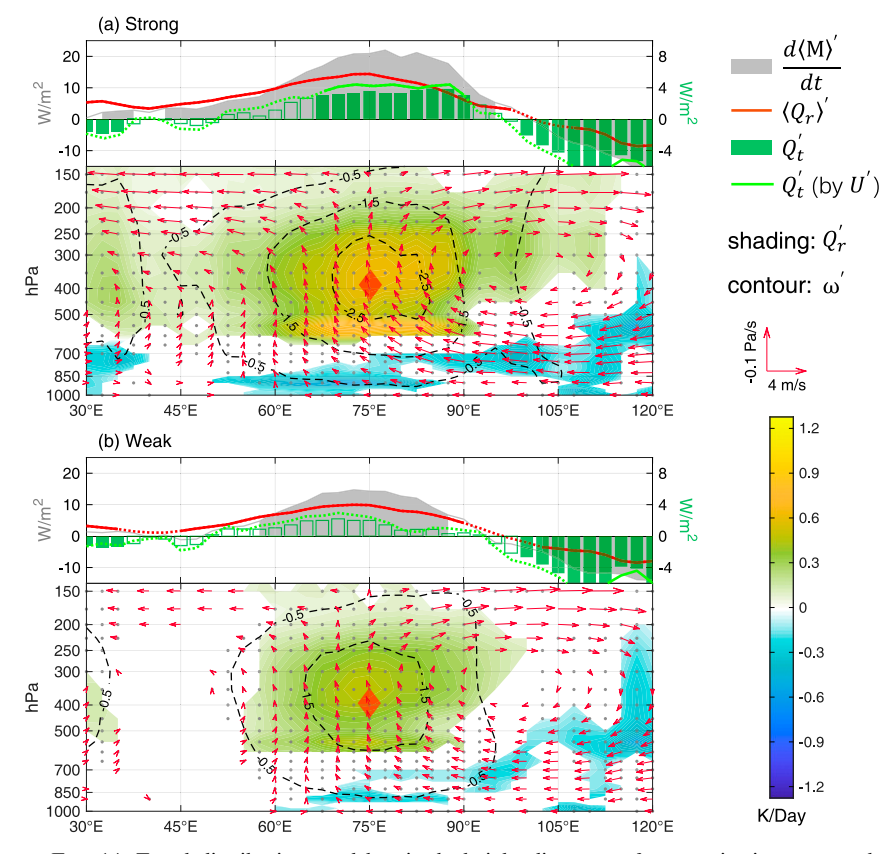


FIG. 14. Zonal distributions and longitude-height diagrams of composite intraseasonal anomalies averaged over 15°S–10°N for the (a) Strong and (b) Weak groups when the MJO convections are centered around 75°E (red diamonds). The one-dimensional plots on the top of each panel show the anomalies of total time change rate of column-integrated MSE (gray area), column-integrated radiative heating (red lines), sum of surface upward sensible and latent heat fluxes (green bars), and its near-surface wind speed related component (green lines). Filled areas and bars and solid lines denote statistically significant signals at the 95% confidence level. The longitude-height diagrams at the bottom of each panel show the radiative heating (shading), vertical pressure velocity (contours, unit: Pa s⁻¹), and vertically overturning circulation (vectors) anomalies. The shading, dotted areas of the contours, and vectors denote statistically significant signals at the 95% confidence level.

comprehensive study on the MJO diversities in terms of both propagation and intensity with observations and reanalysis data. Rather than the Hovmöller diagrams of temporal-filtered OLR anomalies applied in Wang et al. (2019), we performed the cluster analysis for maximum intensity, zonal extent, and mean phase speed of the MJO events that are identified by spatial—temporal-filtered signals. The clustering result reveals four types of MJOs: Strong-Short-Slow, Strong-Long-Fast, Weak-Short-Slow, and Weak-Long-Fast. It is found that the MJO intensity and propagation features are relatively independent of each other, whereas in regard to the propagation a longer zonal extent is often associated with a faster phase speed. The original clusters are thus recombined to explore the factors controlling the MJO propagation and intensity diversities separately.

The propagation diversity is associated with distinct MJO structures, and is connected to the background SSTA and accompanied convective activity changes over the equatorial

Pacific. In contrast to the Short-Slow MJOs, the Long-Fast group has a more intense vertically overturning circulation response to the east of the convection center, which favors both greater MSE tendency leading and greater boundary layer moisture leading that promote a faster eastward phase speed. As a potential mechanism, we argue that an El Niño-like background SSTA pattern and the accompanying convection enhancement over the central Pacific allow a negative diabatic heating anomaly in the existence of an initial subsidence perturbation, amplifying the vertically overturning circulation anomaly to the east of the MJO through positive circulationconvection feedback. The warmer SSTA also provides favorable conditions for the MJOs intruding into the western and central Pacific, favoring a larger zonal extent. Unlike previous studies that emphasized the Kelvin wave response (e.g., Wang et al. 2019; Wei and Ren 2019; Chen and Wang 2020), we argue that the strengthened Kelvin wave response and low-level easterly anomaly in the Long-Fast group are components of the enhanced vertically overturning circulation. In addition to the horizontal and low-level processes, the vertical advection also contributes significantly to the MSE tendency leading, while the location of which shifts eastward relative to the horizontal advections.

The MJO intensity diversity is associated with the interannual SSTA over the Maritime Continent and the background moisture condition over the tropical Indian Ocean where the MJO initiates and develops. An observed interannual warm SSTA over the Maritime Continent leads to an enhanced convection in situ and a strengthened Walker cell with a subsidence over the Indian Ocean. The latter together with the equatorward flow of the Rossby wave response to the enhanced convection are possible causes of the drier background that weakens the MJO intensity. In contrast, a stronger MJO occurs when such a dry condition does not appear. An initial intensity difference amplifies as the MJO propagating eastward through a self-feedback mechanism that combines cloudradiative and WISHE feedbacks. A stronger MJO corresponds with more cloud covers (atmospheric water vapor) and higher near-surface wind speed, which contribute to a larger total time change rate of column-integrated MSE through modifying radiative heating and surface upward heat fluxes, respectively. In this case, a stronger MJO would have a larger intensity growth speed than a weaker one, causing a greater intensity contrast when the MJO is mature over the eastern Indian Ocean.

It is worth pointing out that uncertainties exist in the MJO diversity research. The primary uncertainty comes from the cluster analysis, which is sensitive to the variables for clustering, and to the parameters such as the distance metrics, linkage methods, and number of clusters. In the current work, instead of directly applying the Hovmöller diagrams, we use only three variables to delineate an MJO event such that the information contained in a Hovmöller diagram is extracted and concentrated. In addition, we checked several hundred of clustering results with different combinations of parameters, so as to find out an optimum one with the help of objective criteria (dendrogram or silhouette). Regarding the causes of the MJO diversities, as in many previous studies, we generally focused on the MJO developing and mature phases over the eastern Indian Ocean. However, the MJO structure and background circulations might change in its entire life cycle, such that the causes of the MJO diversities could be regional dependent. Besides, all the conclusions of the current work are based on the latest reanalyses or observations. Numerical experiments are required to confirm these findings, and to answer more in-depth questions. For instance, how the background states are manifested in the self-feedback mechanism. The above issues will be addressed in our future work.

Acknowledgments. This work was jointly supported by NSFC Grant 42088101, NOAA NA18OAR4310298, and NSF AGS-2006553. This is SOEST Contribution Number 11368 and IPRC Contribution Number 1528. The OLR data are provided by the NOAA/OAR/ESRL PSL, Boulder, Colorado, USA, from their Web site at https://psl.noaa.gov/. The ERA5 dataset

is available at Copernicus Climate Change Service Climate Data Store (CDS), https://cds.climate.copernicus.eu/#!/search? text=ERA5&type=dataset. The NOAA NCEI GHRSST Level-4 OI-SST v2.1 dataset is available at https://podaac.jpl.nasa.gov/dataset/AVHRR_OI-NCEI-L4-GLOB-v2.1.

REFERENCES

- Adames, Á. F., and D. Kim, 2016: The MJO as a dispersive, convectively coupled moisture wave: Theory and observations. *J. Atmos. Sci.*, **73**, 913–941, https://doi.org/10.1175/JAS-D-15-0170.1
- Chen, G., and B. Wang, 2019: Dynamic moisture mode versus moisture mode in MJO dynamics: Importance of the wave feedback and boundary layer convergence feedback. *Climate Dyn.*, **52**, 5127–5143, https://doi.org/10.1007/s00382-018-4433-7.
- —, and —, 2020: Circulation factors determining the propagation speed of the Madden–Julian oscillation. *J. Climate*, 33, 3367–3380, https://doi.org/10.1175/JCLI-D-19-0661.1.
- Chen, X., J. Ling, and C. Li, 2016: Evolution of the Madden–Julian oscillation in two types of El Niño. J. Climate, 29, 1919–1934, https://doi.org/10.1175/JCLI-D-15-0486.1.
- Deng, L., T. Li, J. Liu, and M. Peng, 2016: Factors controlling the interannual variations of MJO intensity. J. Meteor. Res., 30, 328–340, https://doi.org/10.1007/s13351-016-5113-3.
- Emanuel, K. A., 1987: An air-sea interaction model of intraseasonal oscillations in the tropics. *J. Atmos. Sci.*, **44**, 2324–2340, https://doi.org/10.1175/1520-0469(1987)044<2324: AASIMO>2.0.CO;2.
- Everitt, B. S., S. Landau, M. Leese, and D. Stahl, 2011: *Cluster Analysis*. Wiley, 346 pp.
- Feng, J., T. Li, and W. Zhu, 2015a: Propagating and nonpropagating MJO events over the Maritime Continent. *J. Climate*, **28**, 8430–8449, https://doi.org/10.1175/JCLI-D-15-0085.1.
- —, P. Liu, W. Chen, and X. Wang, 2015b: Contrasting Madden– Julian oscillation activity during various stages of EP and CP El Niños. Atmos. Sci. Lett., 16, 32–37, https://doi.org/10.1002/asl2.516.
- Fink, A., and P. Speth, 1997: Some potential forcing mechanisms of the year-to-year variability of the tropical convection and its intraseasonal (25–70-day) variability. *Int. J. Climatol.*, **17**, 1513–1534, https://doi.org/10.1002/(SICI) 1097-0088(19971130)17:14<1513::AID-JOC210>3.0.CO;2-U.
- Fuchs, Ž., and D. J. Raymond, 2017: A simple model of intraseasonal oscillations. J. Adv. Model. Earth Syst., 9, 1195–1211, https://doi.org/10.1002/2017MS000963..
- Fuchs-Stone, Ž., 2020: WISHE-moisture mode in a vertically resolved model. J. Adv. Model. Earth Syst., 12, e2019MS001839, https://doi.org/10.1029/2019MS001839.
- Gill, A. E., 1980: Some simple solutions for heat-induced tropical circulation. *Quart. J. Roy. Meteor. Soc.*, **106**, 447–462, https:// doi.org/10.1002/qj.49710644905.
- Gutzler, D. S., 1991: Interannual fluctuations of intraseasonal variance of near-equatorial zonal winds. *J. Geophys. Res. Oceans*, **96**, 3173–3185, https://doi.org/10.1029/90JD01831.
- —, and R. A. Madden, 1989: Seasonal variations in the spatial structure of intraseasonal tropical wind fluctuations. *J. Atmos. Sci.*, 46, 641–660, https://doi.org/10.1175/1520-0469(1989)046<0641:SVITSS>2.0.CO;2.
- Hendon, H. H., and M. L. Salby, 1994: The life cycle of the Madden– Julian oscillation. J. Atmos. Sci., 51, 2225–2237, https://doi.org/ 10.1175/1520-0469(1994)051<2225:TLCOTM>2.0.CO;2.

- —, C. Zhang, and J. D. Glick, 1999: Interannual variation of the Madden–Julian oscillation during austral summer. J. Climate, 12, 2538–2550, https://doi.org/10.1175/1520-0442(1999)012<2538:IVOTMJ>2.0.CO;2.
- Hersbach, H., and Coauthors, 2020: The ERA5 global reanalysis. *Quart. J. Roy. Meteor. Soc.*, **146**, 1999–2049, https://doi.org/10.1002/qj.3803.
- Hsu, P., and T. Li, 2012: Role of the boundary layer moisture asymmetry in causing the eastward propagation of the Madden– Julian oscillation. *J. Climate*, 25, 4914–4931, https://doi.org/ 10.1175/JCLI-D-11-00310.1.
- Hu, F., T. Li, J. Gao, and L. Hao, 2021: Reexamining the moisture mode theories of the Madden–Julian oscillation based on observational analyses. J. Climate, 34, 839–853, https://doi.org/ 10.1175/JCLI-D-20-0441.1.
- Hu, Q., and D. A. Randall, 1994: Low-frequency oscillations in radiative-convective systems. J. Atmos. Sci., 51, 1089–1099, https:// doi.org/10.1175/1520-0469(1994)051<1089:LFOIRC>2.0.CO;2.
- —, and —, 1995: Low-frequency oscillations in radiative-convective systems. Part II: An idealized model. *J. Atmos. Sci.*, **52**, 478–490, https://doi.org/10.1175/1520-0469(1995) 052<0478:LFOIRC>2.0.CO;2.
- Inness, P. M., and J. M. Slingo, 2003: Simulation of the Madden–Julian oscillation in a coupled general circulation model. Part I: Comparison with observations and an atmosphere-only GCM. J. Climate, 16, 345–364, https://doi.org/10.1175/1520-0442(2003)016<0345:SOTMJO>2.0.CO;2.
- Izumo, T., and Coauthors, 2010: Low and high frequency Madden– Julian oscillations in austral summer: Interannual variations. Climate Dyn., 35, 669–683, https://doi.org/10.1007/s00382-009-0655-z.
- Kaufman, L., and P. J. Rousseeuw, 2005: Finding Groups in Data: An Introduction to Cluster Analysis. Wiley, 342 pp.
- Kiladis, G. N., and Coauthors, 2014: A comparison of OLR and circulation-based indices for tracking the MJO. *Mon. Wea. Rev.*, 142, 1697–1715, https://doi.org/10.1175/MWR-D-13-00301.1.
- Kim, D., J. Kug, and A. H. Sobel, 2014: Propagating versus non-propagating Madden–Julian oscillation events. *J. Climate*, 27, 111–125, https://doi.org/10.1175/JCLI-D-13-00084.1.
- ——, H. Kim, and M. I. Lee, 2017: Why does the MJO detour the Maritime Continent during austral summer? *Geophys. Res. Lett.*, 44, 2579–2587, https://doi.org/10.1002/2017GL072643.
- Kim, H., F. Vitart, and D. E. Waliser, 2018: Prediction of the Madden–Julian oscillation: A review. J. Climate, 31, 9425–9443, https://doi.org/10.1175/JCLI-D-18-0210.1.
- Lau, K. M., and P. H. Chan, 1986: The 40–50 day oscillation and the El Niño/Southern oscillation: A new perspective. *Bull. Amer. Meteor. Soc.*, **67**, 533–534, https://doi.org/10.1175/1520-0477(1986)067<0533:TDOATE>2.0.CO;2.
- Li, T., 2014: Recent advance in understanding the dynamics of the Madden–Julian oscillation. J. Meteor. Res., 28 (1), 1–33, https:// doi.org/10.1007/s13351-014-3087-6.
- —, and F. Hu, 2019: A coupled moisture-dynamics model of the Madden–Julian oscillation: Convection interaction with first and second baroclinic modes and planetary boundary layer. Climate Dyn., 53, 5529–5546, https://doi.org/10.1007/s00382-019-04879-x.
- ——, C. Zhao, P. Hsu, and T. Nasuno, 2015: MJO initiation processes over the tropical Indian Ocean during DYNAMO/CINDY2011. J. Climate, 28, 2121–2135, https://doi.org/10.1175/JCLI-D-14-00328.1.
- —, and Coauthors, 2018: A paper on the tropical intraseasonal oscillation published in 1963 in a Chinese journal. Bull. Amer.

- Meteor. Soc., 99, 1765–1779, https://doi.org/10.1175/BAMS-D-17-0216.1.
- —, J. Ling, and P. Hsu, 2020: Madden–Julian oscillation: Its discovery, dynamics, and impact on East Asia. *J. Meteor. Res.*, 34, 20–42, https://doi.org/10.1007/s13351-020-9153-3.
- Liebmann, B., and C. A. Smith, 1996: Description of a complete (interpolated) outgoing longwave radiation dataset. *Bull. Amer. Meteor. Soc.*, 77, 1275–1277, https://doi.org/10.1175/1520-0477-77.6.1274.
- Lin, J., B. Mapes, M. Zhang, and M. Newman, 2004: Stratiform precipitation, vertical heating profiles, and the Madden–Julian oscillation. J. Atmos. Sci., 61, 296–309, https://doi.org/10.1175/ 1520-0469(2004)061<0296:SPVHPA>2.0.CO;2.
- Madden, R. A., and P. R. Julian, 1971: Detection of a 40–50 day oscillation in the zonal wind in the tropical Pacific. *J. Atmos. Sci.*, **28**, 702–708, https://doi.org/10.1175/1520-0469(1971)028<0702:DOADOI>2.0.CO;2.
- —, and —, 1972: Description of global-scale circulation cells in the tropics with a 40–50 day period. *J. Atmos. Sci.*,
 29, 1109–1123, https://doi.org/10.1175/1520-0469(1972) 029<1109:DOGSCC>2.0.CO;2.
- —, and —, 1994: Observations of the 40–50-day tropical oscillation—A review. *Mon. Wea. Rev.*, **122**, 814–837, https://doi.org/10.1175/1520-0493(1994)122<0814:OOTDTO> 2.0,CO:2.
- Maloney, E. D., 2009: The moist static energy budget of a composite tropical intraseasonal oscillation in a climate model. *J. Climate*, 22, 711–729, https://doi.org/10.1175/2008JCLI2542.1.
- Neelin, J. D., and I. M. Held, 1987: Modeling tropical convergence based on the moist static energy budget. *Mon. Wea. Rev.*, **115**, 3–12, https://doi.org/10.1175/1520-0493(1987) 115<0003:MTCBOT>2.0.CO;2.
- Pohl, B., and A. J. Matthews, 2007: Observed changes in the lifetime and amplitude of the Madden–Julian oscillation associated with interannual ENSO sea surface temperature anomalies. *J. Climate*, **20**, 2659–2674, https://doi.org/10.1175/JCLI4230.1.
- Raymond, D. J., and Ž. Fuchs, 2009: Moisture modes and the Madden–Julian oscillation. J. Climate, 22, 3031–3046, https:// doi.org/10.1175/2008JCL12739.1.
- Reynolds, R. W., T. M. Smith, C. Liu, D. B. Chelton, K. S. Casey, and M. G. Schlax, 2007: Daily high-resolution-blended analyses for sea surface temperature. *J. Climate*, **20**, 5473–5496, https://doi.org/10.1175/2007JCLI1824.1.
- Rui, H., and B. Wang, 1990: Development characteristics and dynamic structure of tropical intraseasonal convection anomalies. J. Atmos. Sci., 47, 357–379, https://doi.org/10.1175/1520-0469(1990)047<0357:DCADSO>2.0.CO;2.
- Salby, M. L., and H. H. Hendon, 1994: Intraseasonal behavior of clouds, temperature, and motion in the tropics. J. Atmos. Sci., **51**, 2207–2224, https://doi.org/10.1175/1520-0469(1994)051<2207:IBOCTA>2.0.CO;2.
- Sobel, A., and E. Maloney, 2013: Moisture modes and the eastward propagation of the MJO. *J. Atmos. Sci.*, **70**, 187–192, https://doi.org/10.1175/JAS-D-12-0189.1.
- Sperber, K. R., 2003: Propagation and the vertical structure of the Madden–Julian oscillation. Mon. Wea. Rev., 131, 3018–3037, https:// doi.org/10.1175/1520-0493(2003)131<3018:PATVSO>2.0.CO:2.
- Suematsu, T., and H. Miura, 2018: Zonal SST difference as a potential environmental factor supporting the longevity of the Madden–Julian oscillation. *J. Climate*, 31, 7549–7564, https://doi.org/10.1175/JCLI-D-17-0822.1.
- Tam, C., and N. Lau, 2005: Modulation of the Madden–Julian oscillation by ENSO: Inferences from observations and GCM

- simulations. *J. Meteor. Soc. Japan*, **83**, 727–743, https://doi.org/10.2151/jmsj.83.727.
- Vitart, F., and Coauthors, 2017: The subseasonal to seasonal (S2S) prediction project database. *Bull. Amer. Meteor. Soc.*, **98**, 163–173, https://doi.org/10.1175/BAMS-D-16-0017.1.
- Wang, B., 1988: Comments on "An air–sea interaction model of intraseasonal oscillation in the tropics." J. Atmos. Sci., 45, 3521–3525, https://doi.org/10.1175/1520-0469(1988)045<3521: COAIMO>2.0.CO;2.
- —, and H. Rui, 1990: Synoptic climatology of transient tropical intraseasonal convection anomalies: 1975–1985. *Meteor. Atmos. Phys.*, 44, 43–61, https://doi.org/10.1007/BF01026810.
- —, and T. Li, 1994: Convective interaction with boundary-layer dynamics in the development of a tropical intraseasonal system. *J. Atmos. Sci.*, **51**, 1386–1400, https://doi.org/10.1175/ 1520-0469(1994)051<1386:CIWBLD>2.0.CO;2.
- —, G. Chen, and F. Liu, 2019: Diversity of the Madden–Julian oscillation. Sci. Adv., 5, eaax0220, https://doi.org/10.1126/sciadv.aax0220.
- Wang, L., and T. Li, 2020: Reexamining the MJO moisture mode theories with normalized phase evolutions. *J. Climate*, 33, 8523–8536, https://doi.org/10.1175/JCLI-D-20-0202.1.
- —, —, E. Maloney, and B. Wang, 2017: Fundamental causes of propagating and nonpropagating MJOs in MJOTF/GASS models. J. Climate, 30, 3743–3769, https://doi.org/10.1175/ JCLI-D-16-0765.1.
- —, —, L. Chen, S. K. Behera, and T. Nasuno, 2018: Modulation of the MJO intensity over the equatorial western Pacific by two types of El Niño. *Climate Dyn.*, **51**, 687–700, https://doi.org/10.1007/s00382-017-3949-6.
- Wang, T., and T. Li, 2020: Diagnosing the column-integrated moist static energy budget associated with the northward-propagating boreal summer intraseasonal oscillation. *Climate Dyn.*, **54**, 4711–4732, https://doi.org/10.1007/s00382-020-05249-8.
- ——, X. Yang, J. Fang, X. Sun, and X. Ren, 2018: Role of air–sea interaction in the 30–60-day boreal summer intraseasonal oscillation over the western North Pacific. *J. Climate*, 31, 1653–1680, https://doi.org/10.1175/JCLI-D-17-0109.1.

- —, C. Chu, X. Sun, and T. Li, 2020: Improving real-time forecast of intraseasonal variabilities of Indian summer monsoon precipitation in an empirical scheme. *Front. Earth Sci.*, 8, 577311, https://doi.org/10.3389/feart.2020.577311.
- Ward, J. H., 1963: Hierarchical grouping to optimize an objective function. J. Amer. Stat. Assoc., 58, 236–244, https://doi.org/ 10.1080/01621459.1963.10500845.
- Wei, Y., and H. Ren, 2019: Modulation of ENSO on fast and slow MJO modes during boreal winter. J. Climate, 32, 7483–7506, https://doi.org/10.1175/JCLI-D-19-0013.1.
- Wheeler, M., and G. N. Kiladis, 1999: Convectively coupled equatorial waves: Analysis of clouds and temperature in the wavenumber–frequency domain. *J. Atmos. Sci.*, **56**, 374–399, https://doi.org/10.1175/1520-0469(1999)056<0374:CCEWAO> 2.0.CO;2.
- Wierzchon, S., and M. Klopotek, 2018: *Modern Algorithms of Cluster Analysis*. Springer, 421 pp.
- Xie, Y., S. Chen, Y. Zhang, and Y. Huang, 1963: A preliminarily statistic and synoptic study about the basic currents over southeastern Asia and the initiation of typhoon (in Chinese). Acta Meteor. Sin., 33, 206–217.
- Yanai, M., S. Esbensen, and J. Chu, 1973: Determination of bulk properties of tropical cloud clusters from large-scale heat and moisture budgets. J. Atmos. Sci., 30, 611–627, https://doi.org/ 10.1175/1520-0469(1973)030<0611:DOBPOT>2.0.CO:2.
- Zhang, C., 2005: Madden–Julian oscillation. Rev. Geophys., 43, RG2003, https://doi.org/10.1029/2004RG000158.
- —, 2013: Madden–Julian oscillation: Bridging weather and climate. Bull. Amer. Meteor. Soc., 94, 1849–1870, https://doi.org/10.1175/BAMS-D-12-00026.1.
- —, and J. Ling, 2017: Barrier effect of the Indo-Pacific Maritime Continent on the MJO: Perspectives from tracking MJO precipitation. J. Climate, 30, 3439–3459, https://doi.org/10.1175/ JCLI-D-16-0614.1.
- Zhao, C., T. Li, and T. Zhou, 2013: Precursor signals and processes associated with MJO initiation over the tropical Indian Ocean. J. Climate, 26, 291–307, https://doi.org/10.1175/JCLI-D-12-00113.1.